ACS OMEGA

http://pubs.acs.org/journal/acsodf

Article

Facile Ball-Milling Synthesis of CuO/Biochar Nanocomposites for Efficient Removal of Reactive Red 120

Xiaoqian Wei, Xin Wang, Bin Gao, Weixin Zou,* and Lin Dong*

Cite This: *ACS Omega* 2020, 5, 5748−5755

Read Online

ACCESS | Metrics & More | Article Recommendations | Supporting Information

ABSTRACT: With the goal of improving the removal of anionic contaminants, copper oxide (CuO)-modified biochar (BC) nanocomposites were successfully prepared through simply ball milling CuO particles with BC. The physicochemical properties of the fabricated CuO/BC nanocomposites were systematically characterized by a series of techniques; their adsorption performances were assessed, and the main adsorption mechanism was revealed. X-ray powder diffraction, Fourier transform infrared spectroscopy, and X-ray photoelectron spectroscopy analyses of the nanocomposites showed the strong interaction between CuO and BC and confirmed the success of the ball-milling syntheses. Because of strong electrostatic attraction between the embedded CuO nanoparticles and reactive red (RR120), the composited adsorbents exhibited excellent RR120 removal. The 10%-CuO/BC nanocomposite achieved the best RR120 removal efficiency (46%), which is much higher than that of pristine BC (20%). In addition, the adsorption was insensitive to the change of solution initial pH (4−10). The 10%-CuO/BC also showed fast adsorption kinetics (equilibrium time < 3 h) and extremely high adsorption capacity (Langmuir maximum capacity of 1399 mg g^{-1}) to RR120 in aqueous solutions. Findings from this study demonstrate not only the strong feasibility of ball-milling synthesis of BC-based nanocomposites but also the promising potential of the CuO/BC nanocomposites to remove aqueous anionic contaminants.

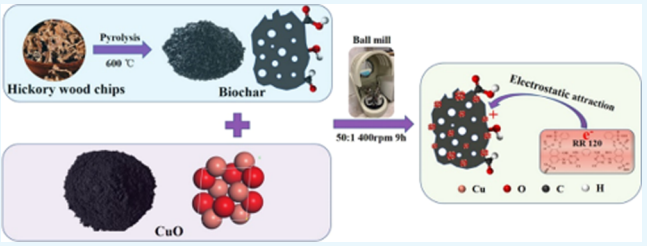

1. INTRODUCTION

Biochar (BC) is an emerging carbonaceous and porous material formed via pyrolysis of a wide range of organic matters such as crop straw, manure, municipal waste, and industrial byproducts under oxygen-limited conditions. It has dramatically attracted attention in agriculture, climate change mitigation, energy production, and environmental remediation.[1−4] Owing to its advantageous properties including large surface area, high porosity, abundant surface functional groups, rich aromaticity, relatively low cost, as well as excellent ion exchange capacity, BC is regarded as a practical alternative cost-effective adsorbent to eliminate both organic and inorganic pollutants (i.e., heavy metals, organic compounds, and possibly nutrients).[5−7]

In comparison to other engineered carbonaceous adsorbents such as activated carbon, pristine/virgin BC often has lower adsorption capacity to a range of aqueous contaminants, especially organics and heavy metals. Moreover, recent studies have demonstrated that pristine BC exhibits little adsorption ability to anionic species (e.g., reactive red dye) in water because its surface is often negatively charged under natural conditions.[8,9] The modification of BC with nanosized metal oxides to form nanocomposites thus has been proposed as an effective way to enhance BC's adsorption properties.[10]

Numerous research studies have shown that the introduction of metal oxide particles onto BC can enhance its sorption capacity to various aqueous pollutants.[11] On one hand, metal oxides on a BC surface may serve as positively charged sorption sites and thus increase the removal of anionic contaminants by the composites.[12] On the other hand, BC with a porous structure can support the distribution and stabilization of metal oxide particles in the nanocomposites.[13] Currently, metal oxide BC composites are mainly produced through two routes including pretreatment of biomass using metal oxide precursors and post-treatment of BC to introduce metal oxide particles.[14,15] For instance, Zhang et al. prepared MgO/BC nanocomposites using $MgCl_2 \cdot 6H_2O$ as the precursor via a one-pot direct pyrolysis method and the resultant nanocomposites showed excellent ionic contamination removal efficiencies.[16] Yao et al. pyrolyzed Mg-enriched tomato tissues to obtain a novel engineered BC with strong adsorption ability to phosphate in aqueous solutions.[17] Cope et al. used an evaporative method to amend iron oxide particles into BC and the composite showed approximately 2 orders of magnitude higher arsenate adsorptive level than an iron oxide-modified sand.[18] These methods require metallic solution impregnation

Received: November 6, 2019
Accepted: January 27, 2020
Published: March 11, 2020

https://dx.doi.org/10.1021/acsomega.9b03787
ACS Omega 2020, 5, 5748−5755

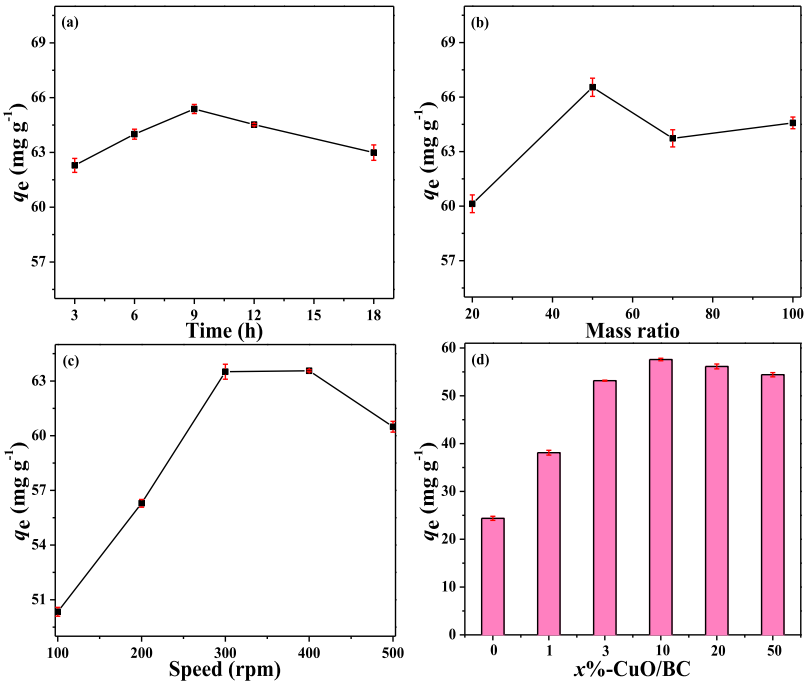

Figure 1. RR120 sorption capacity onto CuO prepared with different milling (a) time, (b) mass ratio, and (c) speed; and (d) effect of CuO content on RR120 adsorption onto CuO/BC nanocomposites.

and copyrolysis processes, which discharge wastewater and gas emission, and thus impose contamination risks to the environment.[19]

High-energy ball milling, a mechanochemistry activation process, has gained considerable attention recently in the fabrication of novel engineered nanomaterials including nanocomposites under solvent-free conditions.[20] Ball milling can reduce particle size and increase specific surface area (SSA), thereby introducing new active edge sites to improve adsorption capacity.[21,22] Shan et al. successfully synthesized two magnetic nanocomposites, BC/Fe_3O_4 and activated carbon/Fe_3O_4, via the ball-milling method.[23] Gu et al. prepared a ZnO@sulphur/carbon nanotube nanocomposite through the ball-milling method and the nanocomposite was applied as a cathode material for high-performance Li−S batteries.[24]

Copper oxide (CuO), a great p-type semiconductor with a narrow band gap of 1.2 eV, has attracted full attention as a capable photocatalyst under irradiation of sunlight.[25] Several studies have indicated that BC modified with CuO can increase the porosity,[26] enlarge the surface area,[27] reduce the sensitivity of BC to solution pH value,[28] and introduce hydrophilic environment over BC.[29] All these changes could improve the adsorption capacity of BC to different kinds of aqueous contaminants. To the best of our knowledge, however, none of the previous studies has used the ball-milling method to synthesize CuO/BC nanocomposites.

As the first of its kind, we synthesized novel CuO/BC nanocomposites using a facile solvent-free ball-milling method and evaluated their sorption performances. An anionic dye, reactive red 120 (RR120), was selected as a model contaminant compound because of its frequent occurrence in colored effluents and easy detection. RR120 is widely used in industrial sectors, and relatively hard to degrade because of its large molecular weight and complex aromatic structure.[30] The objectives of this work are to: (1) optimize ball-milling conditions of CuO/BC nanocomposites; (2) characterize their physicochemical properties; and (3) determine the adsorption behaviors and mechanisms of RR120 on CuO/BC nanocomposites.

2. RESULTS AND DISCUSSION

2.1. Optimal Ball-Milling Parameters and Comparison of Adsorbents. Because CuO was the modification agent of the nanocomposites, the ball-milling conditions were optimized based on the sorption capacity of CuO to RR120. CuO powder were ball milled under different combinations of ball-milling time, speed, and agate ball-to-CuO mass ratio. The adsorption capacities of the ball-milled samples to RR120 are shown in Figure 1a−c. Whereas the ball-milling time (Figure 1a) and agate ball-to-CuO mass ratio (Figure 1b) had little effect on RR120 adsorption onto CuO, the milling speed (Figure 1c) showed greater influences. The highest RR120 adsorption capacities under different ball-milling conditions were 65.38, 66.54, and 63.56 mg g^{-1}at a milling time of 9 h, balls-to-CuO weight ratio of 50:1, and speed of 400 rpm, respectively. These conditions were then used to prepare all the subsequent CuO/BC nanocomposites of different CuO contents.

In comparison of BC−BM, all the CuO/BC nanocomposites showed higher removal of RR120 from aqueous solutions, reflecting the strong RR120 adsorption ability of CuO particles in the nanocomposites (Figure 1d). The RR120 adsorption capacity first increased with CuO content and 10%-CuO/BC had the best performance with a RR120 adsorption capacity of 57.59 mg g^{-1}, 58% higher than that of BC−BM (24.37 mg g^{-1}). Further increase of the amount of CuO in the composites, however, reduced the adsorption of RR120 onto the CuO/BC nanocomposites. This was probably due to the aggregation of CuO nanoparticles in the composites when the CuO content was high. The results indicate that 10%-CuO/BC was the optimal composite adsorbent for RR120 under the

https://dx.doi.org/10.1021/acsomega.9b03787
ACS Omega 2020, 5, 5748−5755

tested conditions and thus was main focus of the follow-up characterization and batch sorption experiments.

2.2. Physiochemical Properties. The SSA and total pore volume (PV) of BC−BM, CuO−BM, and all the CuO/BC nanocomposites are summarized in Table 1. The SSA of

Table 1. Textural Properties of the Adsorbents

samples	surface area (m^2 g^{-1})	PV (cm^3 g^{-1})	CuO size (nm)
BC−BM	327.0	0.069	-
CuO−BM	19.1	-	13.8
1%-CuO/BC	330.0	0.081	10.4
3%-CuO/BC	313.4	0.093	10.9
10%-CuO/BC	296.5	0.111	11.4
20%-CuO/BC	191.2	0.060	12.5
50%-CuO/BC	170.7	0.058	12.7

CuO−BM was the lowest (19.1 m^2 g^{-1}) among all the samples, which can be attributed to its nonporous nature. The SSA of BC−BM was very high with a value of 327.0 m^2 g^{-1}, which is similar to the values in the previous study of other ball-milled BC samples.[31] The SSA of 1%-CuO/BC (330.0 m^2 g^{-1}) was similar to that of BC−BM. However, further loading of CuO nanoparticles reduced the SSA of the CuO/BC nanocomposites, which decreased with increasing CuO content (Table 1). This is likely due to CuO particles taking up the interstitial pores of the BC matrix.[32] Among all the adsorbents, 10%-CuO/BC possessed the biggest PV of 0.111 cm^3 g^{-1}, which might contribute to its distinct performance in the adsorption of RR120. The details of the porous structure were exhibited by the N_2 adsorption and desorption isotherms (Figure S1). However, the SSA of 10%-CuO/BC (296.5 m^2 g^{-1}) was not the highest. In addition, the hysteresis loops of all CuO/BC nanocomposites were similar and could not explain why 10%-CuO/BC had a much larger PV than the others. Because CuO nanoparticles were distributed and stabilized on the BC surface within its pore network, we speculate that the arrangement of these nanoparticles could affect the pore structure of the composites or create addition pore spaces, which might contribute to the high PV and strong RR120 adsorption of 10%-CuO/BC.

The surface morphologies and microstructures of the as-prepared BC−BM, CuO−BM and 10%-CuO/BC samples were compared by scanning electron microscopy (SEM)−energy-dispersive X-ray (EDX) analysis. The SEM images showed that the samples were colloidal/nanosized (Figures 2a,c, and S2a). The EDX spectra clearly demonstrated the presence of Cu in the CuO−BM and 10%-CuO/BC samples (Figures S2b and 2d) and no trace of Cu in the BC−BM sample (Figure 2b), suggesting the successful incorporation of CuO nanoparticles into the nanocomposite. The microstructures of the BC−BM and 10%-CuO/BC samples were further examined by the transmission electron microscopy (TEM) analysis (Figure S3). Comparison of the two samples revealed small CuO nanoparticles attached on the surface of the BC (Figure S3b), suggesting ball milling distributed and stabilized CuO nanoparticles in the BC matrix. The SEM−EDX and TEM results indicate that the novel ball-milling method is flexible in preparing BC-based metal oxide nanocomposites.

The X-ray powder diffraction (XRD) pattern of BC−BM sample indexed as amorphous carbon with broad and low intensity of diffraction peak at around 25°, suggesting low crystallinity.[30] The XRD spectrum of CuO−BM showed several peaks at 32.38, 35.54, 38.64, 48.7, 53.47, 58.3, 61.58, 66.08, and 68.13° (Figure 3a), corresponding to (1 1 0), (0 0 2), (2 0 0), (−2 0 2), (0 2 0), (2 0 2), (−1 1 3), (−3 1 1), and (2 2 0) planes, respectively.[33] Moreover, the sharp and narrow diffraction peaks indicated its high crystallinity. These peaks also existed in the XRD pattern for the CuO/BC nanocomposites, suggesting that formation of nanocomposites did not cause notable changes to the crystallinity of CuO. The crystalline size of the CuO crystal plane (0 0 2) in the

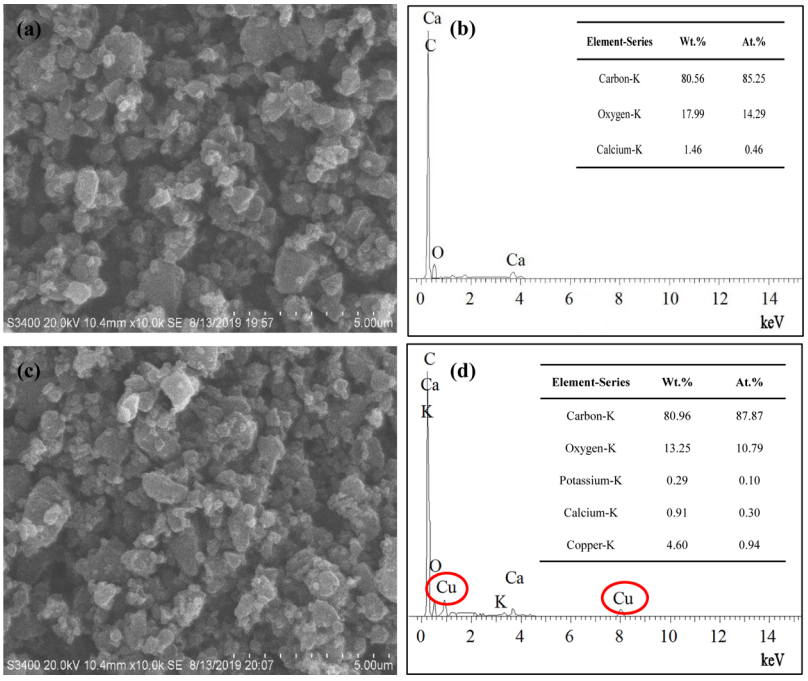

Figure 2. SEM images of (a) BC−BM and (c) 10%-CuO/BC, and EDX spectra of (b) BC−BM and (d) 10%-CuO/BC samples.

https://dx.doi.org/10.1021/acsomega.9b03787
ACS Omega 2020, 5, 5748−5755

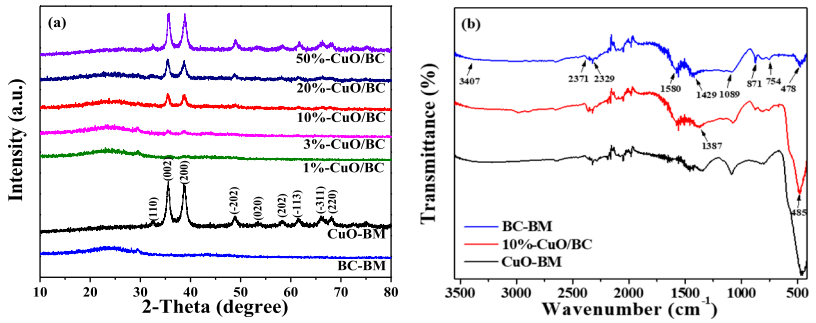

Figure 3. (a) XRD patterns of CuO−BM, BC−BM, and CuO/BC nanocomposites; (b) FT-IR spectra of CuO−BM, BC−BM, and 10%-CuO/BC.

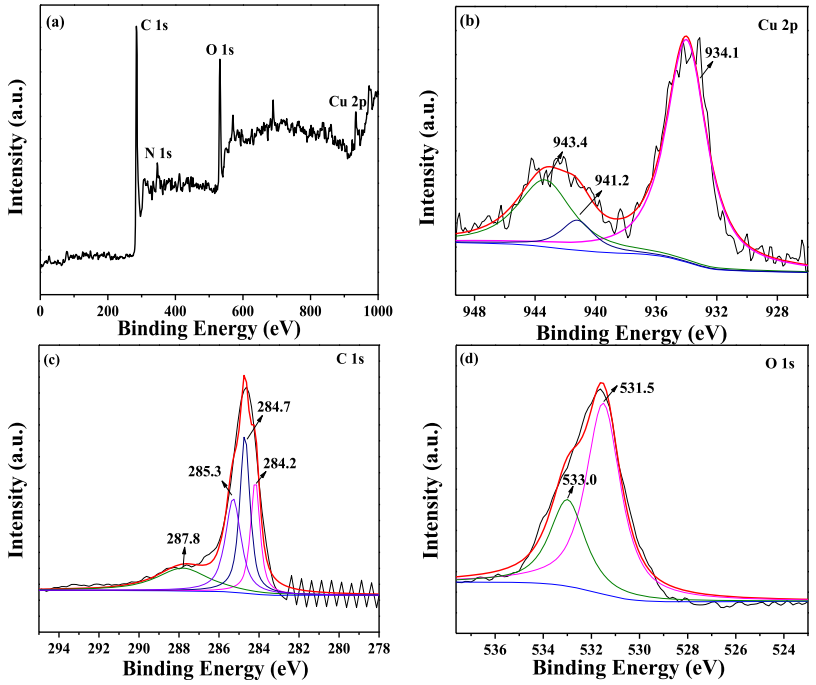

Figure 4. XPS spectra of 10%-CuO/BC: (a) full-range survey, (b) Cu 2p, (c) C 1s, and (d) O 1s.

composites was calculated with the Debye-Scherrer equation. The results confirmed that the CuO particles in the composites were nanosized and in the range of 10−14 nm (Table 1).

The Fourier transform infrared (FT-IR) spectrum of BC−BM showed several absorption peaks at around 3407, 1580, and 478 cm^{-1}, which can be assigned to the stretching mode of O−H and N−H groups, aromatic C═C/C═O groups, and C−O bending deformation, respectively (Figure 3b). In addition, two peaks observed at 1089 and 1429 cm^{-1} can be ascribed to C−O and phenolic O−H, respectively.[20,34] Appearance of the peaks at about 871 and 754 cm^{-1} is primarily characteristic of aromatic C−H bending, whereas the asymmetrical stretching vibration of C−H bonds from C−H and C═C groups appeared at 2371 and 2329 cm^{-1}, respectively.[35] After CuO modification, the 10%-CuO/BC sample showed a sharp vibration peak of the Cu(II)−O bond at 485 cm^{-1}, indicating that the CuO nanoparticles was introduced into the BC with the aid of oxygen functionalities.[36] Furthermore, the peak position of phenolic −OH was slightly shifted from 1429 to 1378 cm^{-1}on the composite, suggesting that Cu(II) might produce a chelation effect with the −OH group.[11]

The characteristic peaks of C 1s, N 1s, O 1s, and Cu 2p were detected in the X-ray photoelectron spectroscopy (XPS) spectrum of 10%-CuO/BC (Figure 4a), confirming the presence of Cu species in the synthesized composite. The Cu 2p spectrum (Figure 4b) exhibited two shakeup satellite peaks at 943.4 and 941.2 eV, attributed to Cu $2p_{3/2}$ and a symmetric primary peak at 934.1 eV ascribed to Cu^{2+} core features, confirming the formation of the CuO phase in the nanocomposite.[37] In the C 1s spectrum (Figure 4c), the peaks located at 287.8, 285.3, 284.7, and 284.2 eV can be indexed to C═O/ketone C, C−O, C−H, and C═C/C−C, respectively.[11,38] As for the O 1s spectrum (Figure 4d), the broad peak was fitted into the two significant peaks centered at 533.0 eV (C−O−C/C−O−H) and 531.5 eV (−OH/Cu−O).[35,39] In comparison of those of CuO−BM and BC−BM (Figure S4), the binding energies of Cu 2p peaks of 10%-CuO/BC slightly shifted to lower values, whereas C 1s and O 1s peaks shifted to higher values, reflecting the interactions between CuO and BC in the nanocomposite. The XPS results also confirmed the success in synthesis of the CuO/BC nanocomposites.

2.3. Adsorption Behaviors. Initial solution pH showed little effect on the adsorption of RR120 onto 10%-CuO/BC and there were no obvious differences among the removal rate

https://dx.doi.org/10.1021/acsomega.9b03787
ACS Omega 2020, 5, 5748−5755

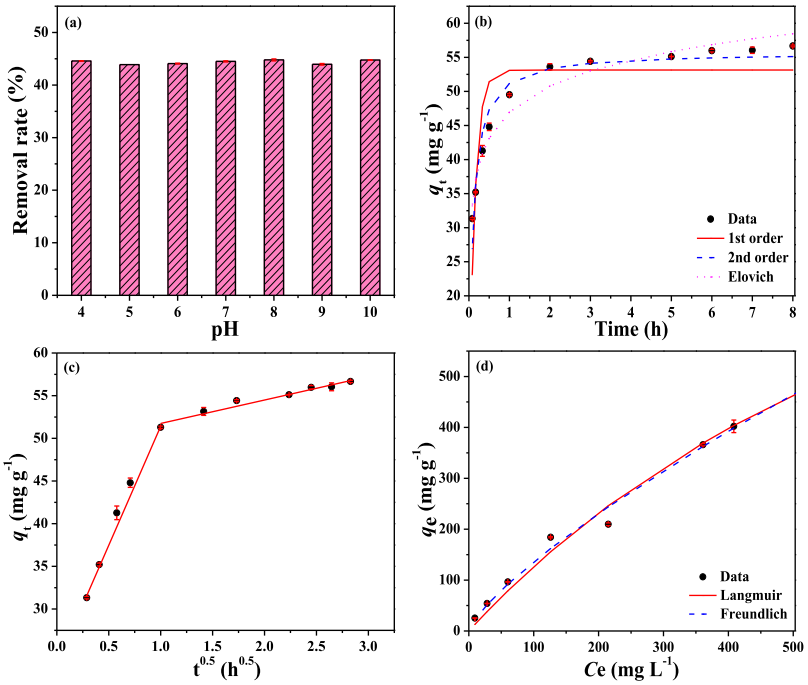

Figure 5. (a) Effect of the solution pH on RR120 adsorption, (b) kinetics of RR120 adsorption (vs time), (c) kinetics of RR120 adsorption (vs square root of time), and (d) isotherms of RR120 adsorption onto 10%-CuO/BC. The lines are simulations of various models.

Table 2. Best-Fit Parameters of the Kinetic and Isotherm Models for RR120 Adsorption Onto 10%-CuO/BC

model	parameter 1	parameter 2	R^2
pseudo-first-order	k_1 = 6.799 h^{-1}	q_e = 53.3 mg g^{-1}	0.767
pseudo-second-order	k_2 = 0.202 g mg^{-1} h^{-1}	q_e = 55.9 mg g^{-1}	0.952
Elovich	α = 28510.712 mg g^{-1} h^{-1}	β = 0.182 g mg^{-1}	0.947
Langmuir	K_L = 0.001 L mg^{-1}	q_m = 1399 mg g^{-1}	0.986
Freundlich	K_f = 4.01 mg$^{(1-n)}$ L^n g^{-1}	n_f = 0.765	0.992

(~45%) at a pH of 4−10 (Figure 5a). Because the point of zero charge of CuO is around 10,[40] the surface of the CuO particles in the nanocomposite was positively charged under most of the tested conditions. As a result, the CuO particles in the nanocomposite would adsorb anionic RR120 through electrostatic attraction,[20] which would explain why the adsorption was insensitive to initial solution pH under the tested conditions. The results also indicate the importance of electrostatic interaction mechanism to the adsorption of RR120 onto CuO/BC nanocomposites.

The adsorption kinetic rate of RR120 onto 10%-CuO/BC increased sharply in the first 0.5 h, then slowed down over time, and reached the adsorption equilibrium within 3 h (Figure 5b). As shown, the equilibrium adsorption capacity of the adsorbent approached approximately 56.67 mg g^{-1} at the initial RR120 concentration of 50 mg L^{-1}. The relatively fast adsorption rate in the initial stage was probably due to the considerable amount of available vacant surface sites on the surface of the CuO/BC nanocomposite boosting electrostatic interaction with RR120 molecules.[41] However, the adsorption rate started to decrease subsequently, owing to the small number of remaining active sites and relatively strong mass transfer resistance under the low concentration gradient of the RR120 solutions.[42]

The adsorption kinetic data were fitted to commonly used kinetic models including the pseudo-first-order, pseudo-second-order, and Elovich models. The descriptions of these models can be found in the Supporting Information (S2) and the best-fit model parameters are listed in Table 2. The pseudo-second-order model (R^2 = 0.952) provided the best fit of the experimental data comparing with the Elovich model (R^2 = 0.947) and the pseudo-first-order model (R^2 = 0.767). These results suggest that the adsorption of RR120 dye onto the nanocomposite was more likely controlled by the chemisorption process and the boundary layer resistance might not act as the rate-limiting step.[43] The plot of the kinetic adsorption data versus $t^{0.5}$ exhibited two segments of straight lines (Figure 5c), suggesting that the adsorption kinetics of RR120 onto the nanocomposites could be controlled by the intraparticle diffusion process.[44]

The 10%-CuO/BC showed a relatively high adsorption of RR120 at a wide range of equilibrium concentrations (Figure 5d), reflecting the large adsorption capacity of the nanocomposite to RR120. The Langmuir and Freundlich models were applied to simulate the experimental isotherms (S3, Supporting Information) and both models worked well with R^2 values larger than 0.986 (Table 2). The fitting of the Freundlich model was slightly better than that of the Langmuir model, probably because of high surface heterogeneity of the nanocomposite.[45] Nevertheless, the Langmuir model still simulated the experimental isotherm very well, suggesting the dominance of the monolayer adsorption behavior.[46] The predicted Langmuir maximum adsorption capacity of the 10%-CuO/BC to RR120 reached 1399 mg g^{-1}, demonstrating the

https://dx.doi.org/10.1021/acsomega.9b03787
ACS Omega 2020, 5, 5748−5755

strong adsorption of the nanocomposite to the anionic dye. The adsorption kinetics and isotherm results suggest that CuO/BC nanocomposites can be utilized as an effective adsorbent for anionic contaminants.

3. CONCLUSIONS

In summary, highly efficient CuO/BC nanocomposites were successfully fabricated from CuO particles and BC via a facile and ecofriendly ball-milling method. The CuO nanoparticles on the BC surface served as positively charged adsorption sites of the nanocomposites to effectively remove an anionic dye (RR120) from aqueous solutions through electrostatic attraction. As a result, 10%-CuO/BC exhibited fast adsorption kinetics and extraordinary adsorption capacity to aqueous RR120. It is anticipated that CuO/BC nanocomposites would hold great promise as an adsorbent in the removal of anionic organic pollutants from contaminated water. Compared to traditional methods, the ball-milling technology is more feasible and has greater potential in practical uses for preparing BC-based nanocomposites.

4. MATERIALS AND METHODS

4.1. Materials. All the chemicals were of analytical grade and used without further purification. Deionized (DI) water (18.2 MΩ, Nanopure, Barnstead) was used throughout the experiments. RR120 ($C_{44}H_{24}C_{l2}N_{14}Na_6O_{20}S_6$) was obtained from Sigma-Aldrich, India. Hickory wood chips (HC) supplied by Cowboy Charcoal, HC was chosen as the feedstock material of pristine BC. CuO powder (97% purity, Belgium) and sodium hydroxide (NaOH) (98.5%, SE) were purchased from Acros Organics. Hydrochloric acid (HCl) (37%, USA) was supplied by Sigma-Aldrich.

4.2. Preparation of Adsorbents. The preparation process of CuO under different ball-milling conditions can be seen in the Supporting Information (S1).

HC was ground into 1−2 mm pieces for BC production. The feedstock was heated in a tubular furnace (Olympic 1823HE) under a N_2 environment and kept for 8 h at a peak temperature of 600 °C. After cooling down to room temperature, the product was rinsed several times using DI water to get rid of the impurities and oven-dried at 80 °C. The sample was labeled as BC.

CuO/BC nanocomposites were synthesized via the ball-milling method. In a typical synthesis procedure, 1.8 g of powder of a mixture of CuO and BC nominal at a weight ratio of 1:99, 1:97, 1:9, 1:4, or 1:1 was put into a planetary ball mill (PQ-N2, Across International, New Jersey, USA) within agate jars, and then 90 g balls were added into each jar. The mass ratio of the balls to the powdered mixture was kept constant at about 50:1 throughout all experiments. Each experiment was employed for 9 h at a speed of 400 rpm in ambient air and the rotation direction was altered every 1.5 h. The obtained nanocomposites were denoted as 1%-CuO/BC, 3%-CuO/BC, 10%-CuO/BC, 20%-CuO/BC, and 50%-CuO/BC, where the percentages are CuO contents. Pristine BC and CuO were ball milled separately under the same conditions and labeled as BC−BM and CuO−BM, respectively.

4.3. Characterization Methods. The obtained BC samples were used directly in most of the characterization analyses. The micromorphology of the adsorbents was characterized by a field emission gun scanning electron microscopy (FEG−SEM, Hitachi S-3400N) equipped with an EDX analyzer. TEM was carried out on a JEM-1011 instrument at an acceleration voltage of 200 kV. For the TEM analysis, the samples were crushed and dispersed in A.R. grade ethanol with ultrasonic treatment and the resulting suspensions were dried on carbon-film-supported copper grids. XRD measurement patterns were obtained on a Philips X'Pert Pro diffractometer by Ni-filtered Cu Kα radiation (λ = 0.15418 nm) at a scanning rate of 10°/min from 10 to 80° to identify the crystallographic structure of the samples. The SSA and PV of the samples were determined according to the Brunauer−Emmet−Teller theory using N_2-adsorption at −196 °C on Micrometrics ASAP-2020 adsorption apparatus. FT-IR was recorded in the range of 400−4000 cm^{-1} with the spectral resolution of 4 cm^{-1} and on a Nicolet 5700 FT-IR spectrometer to detect the surface organic functional groups of the samples. The elemental composition and oxidation state of the samples were determined by XPS analysis on a PHI 5000 Versa Probe high-performance electron spectrometer using an Al Kα radiation (1486.6 eV) achromatic X-ray source.

4.4. Batch Sorption Experiments. A stock solution (1 g L^{-1}) of RR120 was freshly prepared by dissolving 0.5 g of RR120 into 500 mL of DI water. Various RR120 concentrations required in all batch experiments were made by diluting the stock solution.

Batch sorption experiments were carried out to compare the adsorption ability of the samples obtained under various milling conditions at different CuO/BC ratios. About 20 mg of sorbent (dosage of 0.40 g L^{-1}) was added into a 50 mL conical centrifuge tube (Thermo Fisher Scientific, Korea) containing 50 mL of 50 mg L^{-1} RR120 solutions. After shaking for 24 h, the mixtures were immediately withdrawn to determine the removal rates. The sample with the highest RR120 removal rate (10%-CuO/BC) was selected to further investigate the adsorption behaviors of RR120 on CuO/BC nanocomposites.

The effect of initial pH on RR120 removal was investigated using 10%-CuO/BC composite pH = 2−10 (i.e., 2, 3, 4, 5, 6, 7, 8, 9, and 10) under the same conditions (dosage, concentration, and contact time). Negligible volumes of 0.01 M HCl or NaOH solutions were used to adjust the solutions' pH to desired values monitored by a pH meter (Fisher Scientific, AB 15 digital pH meter).

To measure the adsorption kinetics, 0.02 g of 10%-CuO/BC was added into 50 mL of 50 mg L^{-1} RR120 solutions shaking for different time intervals (i.e., 0.08, 0.17, 0.33, 0.5, 1, 2, 3, 5, 6, 7, and 8 h). The isotherms were obtained by adding 0.02 g of the adsorbent with 50 mL RR120 of varying initial concentrations ranging from 20 to 750 mg L^{-1} (i.e., 20, 50, 100, 200, 300, 500, 600, and 750 mg L^{-1}) and shaken for 24 h.

In all experiments, the mixtures were shaken at a constant rate (240 rpm) using a mechanical shaker at room temperature (25 °C). The withdrawn samples were filtered by 0.22 μm pore size nylon membrane filters (MCE Syringe Filter, China). The aqueous RR120 concentrations were analyzed by a UV−vis spectrophotometer (EVO 60, Thermo Fisher Scientific International, USA) at a wavelength of 515 nm. All experiments were performed in duplicate and the average values are reported.

■ ASSOCIATED CONTENT

Supporting Information

The Supporting Information is available free of charge at https://pubs.acs.org/doi/10.1021/acsomega.9b03787.

https://dx.doi.org/10.1021/acsomega.9b03787
ACS Omega 2020, 5, 5748−5755

Preparation of CuO under different ball milling conditions; adsorption kinetic and isotherm models; N_2 adsorption and desorption isotherms for CuO−BM, BC−BM, and CuO/BC composites; SEM image and EDX spectra of the CuO−BM sample; TEM images of BC−BM and 10%-CuO/BC samples; and XPS spectra of CuO−BM: Cu 2p, O 1s, and BC−BM: C 1s, O 1s (PDF)

AUTHOR INFORMATION

Corresponding Authors

Weixin Zou − *Key Laboratory of Mesoscopic Chemistry of MOE, School of Chemistry and Chemical Engineering and Jiangsu Key Laboratory of Vehicle Emissions Control, Center of Modern Analysis, Nanjing University, Nanjing 210093, PR China*; Email: wxzou2016@nju.edu.cn

Lin Dong − *Key Laboratory of Mesoscopic Chemistry of MOE, School of Chemistry and Chemical Engineering, Jiangsu Key Laboratory of Vehicle Emissions Control, Center of Modern Analysis, and School of the Environmental, Nanjing University, Nanjing 210093, PR China*; orcid.org/0000-0002-8393-6669; Email: donglin@nju.edu.cn

Authors

Xiaoqian Wei − *Key Laboratory of Mesoscopic Chemistry of MOE, School of Chemistry and Chemical Engineering and Jiangsu Key Laboratory of Vehicle Emissions Control, Center of Modern Analysis, Nanjing University, Nanjing 210093, PR China; Department of Agricultural and Biological Engineering, University of Florida, Gainesville, Florida 32611, United States*

Xin Wang − *Key Laboratory of Mesoscopic Chemistry of MOE, School of Chemistry and Chemical Engineering and Jiangsu Key Laboratory of Vehicle Emissions Control, Center of Modern Analysis, Nanjing University, Nanjing 210093, PR China*

Bin Gao − *Department of Agricultural and Biological Engineering, University of Florida, Gainesville, Florida 32611, United States*; orcid.org/0000-0003-3769-0191

Complete contact information is available at: https://pubs.acs.org/10.1021/acsomega.9b03787

Notes

The authors declare no competing financial interest.

ACKNOWLEDGMENTS

W.Z. and L.D. would like to acknowledge the support of the National Natural Science Foundation of China (21707066, 21677069, and 21773106).

REFERENCES

(1) Zhu, N.; Yan, T.; Qiao, J.; Cao, H. Adsorption of arsenic, phosphorus and chromium by bismuth impregnated biochar: Adsorption mechanism and depleted adsorbent utilization. *Chemosphere* **2016**, *164*, 32−40.

(2) Gonçalves, S. P. C.; Strauss, M.; Martinez, D. S. T. The Positive Fate of Biochar Addition to Soil in the Degradation of PHBV-Silver Nanoparticle Composites. *Environ. Sci. Technol.* **2018**, *52*, 13845−13853.

(3) Liu, W.-J.; Jiang, H.; Yu, H.-Q. Development of Biochar-Based Functional Materials: Toward a Sustainable Platform Carbon Material. *Chem. Rev.* **2015**, *115*, 12251−12285.

(4) Lee, D.-J.; Cheng, Y.-L.; Wong, R.-J.; Wang, X.-D. Adsorption removal of natural organic matters in waters using biochar. *Bioresour. Technol.* **2018**, *260*, 413−416.

(5) Rodriguez-Narvaez, O. M.; Peralta-Hernandez, J. M.; Goonetilleke, A.; Bandala, E. R. Biochar-supported nanomaterials for environmental applications. *J. Ind. Eng. Chem.* **2019**, *78*, 21−33.

(6) Yang, X.; Zhang, X.; Wang, Z.; Li, S.; Zhao, J.; Liang, G.; Xie, X. Mechanistic insights into removal of norfloxacin from water using different natural iron ore − biochar composites: more rich free radicals derived from natural pyrite-biochar composites than hematite-biochar composites. *Appl. Catal., B* **2019**, *255*, 117752.

(7) Luo, K.; Yang, Q.; Pang, Y.; Wang, D.; Li, X.; Lei, M.; Huang, Q. Unveiling the mechanism of biochar-activated hydrogen peroxide on the degradation of ciprofloxacin. *Chem. Eng. J.* **2019**, *374*, 520−530.

(8) Xu, X.; Zheng, Y.; Gao, B.; Cao, X. N-doped biochar synthesized by a facile ball-milling method for enhanced sorption of CO_2 and reactive red. *Chem. Eng. J.* **2019**, *368*, 564−572.

(9) Zhao, R.; Li, X.; Sun, B.; Ji, H.; Wang, C. Diethylenetriamine-assisted synthesis of amino-rich hydrothermal carbon-coated electrospun polyacrylonitrile fiber adsorbents for the removal of Cr(VI) and 2,4-dichlorophenoxyacetic acid. *J. Colloid Interface Sci.* **2017**, *487*, 297−309.

(10) Tan, X.-f.; Liu, Y.-g.; Gu, Y.-l.; Xu, Y.; Zeng, G.-m.; Hu, X.-j.; Liu, S.-b.; Wang, X.; Liu, S.-m.; Li, J. Biochar-based nano-composites for the decontamination of wastewater: A review. *Bioresour. Technol.* **2016**, *212*, 318−333.

(11) Liu, S.; Xu, W.-h.; Liu, Y.-g.; Tan, X.-f.; Zeng, G.-m.; Li, X.; Liang, J.; Zhou, Z.; Yan, Z.-l.; Cai, X.-x. Facile synthesis of Cu(II) impregnated biochar with enhanced adsorption activity for the removal of doxycycline hydrochloride from water. *Sci. Total Environ.* **2017**, *592*, 546−553.

(12) Dieguez-Alonso, A.; Anca-Couce, A.; Frišták, V.; Moreno-Jiménez, E.; Bacher, M.; Bucheli, T. D.; Cimò, G.; Conte, P.; Hagemann, N.; Haller, A.; Hilber, I.; Husson, O.; Kammann, C. I.; Kienzl, N.; Leifeld, J.; Rosenau, T.; Soja, G.; Schmidt, H.-P. Designing biochar properties through the blending of biomass feedstock with metals: Impact on oxyanions adsorption behavior. *Chemosphere* **2019**, *214*, 743−753.

(13) Rajapaksha, A. U.; Chen, S. S.; Tsang, D. C. W.; Zhang, M.; Vithanage, M.; Mandal, S.; Gao, B.; Bolan, N. S.; Ok, Y. S. Engineered/designer biochar for contaminant removal/immobilization from soil and water: Potential and implication of biochar modification. *Chemosphere* **2016**, *148*, 276−291.

(14) Wang, B.; Gao, B.; Fang, J. Recent advances in engineered biochar productions and applications. *Crit. Rev. Environ. Sci. Technol.* **2018**, *47*, 2158−2207.

(15) Ahmed, M. B.; Zhou, J. L.; Ngo, H. H.; Guo, W.; Chen, M. Progress in the preparation and application of modified biochar for improved contaminant removal from water and wastewater. *Bioresour. Technol.* **2016**, *214*, 836−851.

(16) Zhang, M.; Gao, B.; Yao, Y.; Xue, Y.; Inyang, M. Synthesis of porous MgO-biochar nanocomposites for removal of phosphate and nitrate from aqueous solutions. *Chem. Eng. J.* **2012**, *210*, 26−32.

(17) Yao, Y.; Gao, B.; Chen, J.; Zhang, M.; Inyang, M.; Li, Y.; Alva, A.; Yang, L. Engineered carbon (biochar) prepared by direct pyrolysis of Mg-accumulated tomato tissues: characterization and phosphate removal potential. *Bioresour. Technol.* **2013**, *138*, 8−13.

(18) Cope, C. O.; Webster, D. S.; Sabatini, D. A. Arsenate adsorption onto iron oxide amended rice husk char. *Sci. Total Environ.* **2014**, *488−489*, 554−561.

(19) Zhang, Q.; Yang, L.; Hu, S.; Liu, X.; Duan, X. Consequences of ball-milling treatment on the physicochemical, rheological and emulsifying properties of egg phosvitin. *Food Hydrocolloids* **2019**, *95*, 418−425.

(20) Lyu, H.; Gao, B.; He, F.; Zimmerman, A. R.; Ding, C.; Huang, H.; Tang, J. Effects of ball milling on the physicochemical and sorptive properties of biochar: Experimental observations and governing mechanisms. *Environ. Pollut.* **2018**, *233*, 54−63.

(21) Meng, F.; Ma, W.; Duan, C.; Liu, X.; Chen, Z.; Wang, M.; Gao, J.; Zhang, Z. High efficient degradation of levofloxacin by edge-selectively Fe@3D-WS_2: Self-renewing behavior and Degradation mechanism study. *Appl. Catal., B* **2019**, *252*, 187−197.

(22) Petrović, S.; Rožić, L.; Grbić, B.; Radić, N.; Stefanov, P.; Stojadinović, S.; Jović, V.; Lamovec, J. Effect of high energy ball milling on the physicochemical properties of TiO_2−CeO_2 mixed oxide and its photocatalytic behavior in the oxidation reaction. *React. Kinet., Mech. Catal.* **2019**, *127*, 175−186.
(23) Shan, D.; Deng, S.; Zhao, T.; Wang, B.; Wang, Y.; Huang, J.; Yu, G.; Winglee, J.; Wiesner, M. R. Preparation of ultrafine magnetic biochar and activated carbon for pharmaceutical adsorption and subsequent degradation by ball milling. *J. Hazard. Mater.* **2016**, *305*, 156−163.
(24) Gu, X.; Tong, C.-j.; Wen, B.; Liu, L.-m.; Lai, C.; Zhang, S. Ball-milling synthesis of ZnO@sulphur/carbon nanotubes and $Ni(OH)_2$ @sulphur/carbon nanotubes composites for high-performance lithium-sulphur batteries. *Electrochim. Acta* **2016**, *196*, 369−376.
(25) Bharathi, P.; Harish, S.; Archana, J.; Navaneethan, M.; Ponnusamy, S.; Muthamizhchelvan, C.; Shimomura, M.; Hayakawa, Y. Enhanced charge transfer and separation of hierarchical CuO/ZnO composites: The synergistic effect of photocatalysis for the mineralization of organic pollutant in water. *Appl. Surf. Sci.* **2019**, *484*, 884−891.
(26) Nekouei, F.; Noorizadeh, H.; Nekouei, S.; Asif, M.; Tyagi, I.; Agarwal, S.; Gupta, V. K. Removal of malachite green from aqueous solutions by cuprous iodide-cupric oxide nano-composite loaded on activated carbon as a new sorbent for solid phase extraction: Isotherm, kinetics and thermodynamic studies. *J. Mol. Liq.* **2016**, *213*, 360−368.
(27) Premarathna, K. S. D.; Rajapaksha, A. U.; Sarkar, B.; Kwon, E. E.; Bhatnagar, A.; Ok, Y. S.; Vithanage, M. Biochar-based engineered composites for sorptive decontamination of water: A review. *Chem. Eng. J.* **2019**, *372*, 536−550.
(28) Hu, H.; Sun, L.; Jiang, B.; Wu, H.; Huang, Q.; Chen, X. Low concentration Re(VII) recovery from acidic solution by Cu-biochar composite prepared from bamboo (Acidosasa longiligula) shoot shell. *Miner. Eng.* **2018**, *124*, 123−136.
(29) Rajesh, R.; Iyer, S. S.; Ezhilan, J.; Kumar, S. S.; Venkatesan, R. Graphene oxide supported copper oxide nanoneedles: An efficient hybrid material for removal of toxic azo dyes. *Spectrochim. Acta, Part A* **2016**, *166*, 49−55.
(30) Zheng, Y.; Yang, Y.; Zhang, Y.; Zou, W.; Luo, Y.; Dong, L.; Gao, B. Facile one-step synthesis of graphitic carbon nitride-modified biochar for the removal of reactive red 120 through adsorption and photocatalytic degradation. *Biochar* **2019**, *1*, 89−96.
(31) Zhang, Q.; Wang, J.; Lyu, H.; Zhao, Q.; Jiang, L.; Liu, L. Ball-milled biochar for galaxolide removal: Sorption performance and governing mechanisms. *Sci. Total Environ.* **2019**, *659*, 1537−1545.
(32) Chaukura, N.; Murimba, E. C.; Gwenzi, W. Synthesis, characterisation and methyl orange adsorption capacity of ferric oxide-biochar nano-composites derived from pulp and paper sludge. *Appl. Water Sci.* **2016**, *7*, 2175−2186.
(33) Raizada, A.; Ganguly, D.; Mankad, M. M.; Krishna, R.; Nagabhushana, B. A highly efficient copper oxide nanopowder for adsorption of methylene blue dye from aqueous medium. *J. Chem. Eng. Chem. Res.* **2014**, *2*, 249−258.
(34) Lyu, H.; Tang, J.; Huang, Y.; Gai, L.; Zeng, E. Y.; Liber, K.; Gong, Y. Removal of hexavalent chromium from aqueous solutions by a novel biochar supported nanoscale iron sulfide composite. *Chem. Eng. J.* **2017**, *322*, 516−524.
(35) He, X.; Yang, D.-P.; Zhang, X.; Liu, M.; Kang, Z.; Lin, C.; Jia, N.; Luque, R. Waste eggshell membrane-templated CuO-ZnO nanocomposites with enhanced adsorption, catalysis and antibacterial properties for water purification. *Chem. Eng. J.* **2019**, *369*, 621−633.
(36) El-Trass, A.; ElShamy, H.; El-Mehasseb, I.; El-Kemary, M. CuO nanoparticles: Synthesis, characterization, optical properties and interaction with amino acids. *Appl. Surf. Sci.* **2012**, *258*, 2997−3001.
(37) Zou, W.; Zhang, L.; Liu, L.; Wang, X.; Sun, J.; Wu, S.; Deng, Y.; Tang, C.; Gao, F.; Dong, L. Engineering the Cu_2O−reduced graphene oxide interface to enhance photocatalytic degradation of organic pollutants under visible light. *Appl. Catal., B* **2016**, *181*, 495−503.
(38) Singh, B.; Fang, Y.; Cowie, B. C. C.; Thomsen, L. NEXAFS and XPS characterisation of carbon functional groups of fresh and aged biochars. *Org. Geochem.* **2014**, *77*, 1−10.
(39) Xu, H.; Jiang, H. Effects of cyanobacterial extracellular polymeric substances on the stability of ZnO nanoparticles in eutrophic shallow lakes. *Environ. Pollut.* **2015**, *197*, 231−239.
(40) Chauhan, M.; Sharma, B.; Kumar, R.; Chaudhary, G. R.; Hassan, A. A.; Kumar, S. Green synthesis of CuO nanomaterials and their proficient use for organic waste removal and antimicrobial application. *Environ. Res.* **2019**, *168*, 85−95.
(41) Liu, X.; Zhang, L. Removal of phosphate anions using the modified chitosan beads: Adsorption kinetic, isotherm and mechanism studies. *Powder Technol.* **2015**, *277*, 112−119.
(42) Tanhaei, B.; Ayati, A.; Lahtinen, M.; Sillanpää, M. Preparation and characterization of a novel chitosan/Al_2O_3/magnetite nanoparticles composite adsorbent for kinetic, thermodynamic and isotherm studies of Methyl Orange adsorption. *Chem. Eng. J.* **2015**, *259*, 1−10.
(43) Ahmed, M. B.; Zhou, J. L.; Ngo, H. H.; Guo, W. Adsorptive removal of antibiotics from water and wastewater: Progress and challenges. *Sci. Total Environ.* **2015**, *532*, 112−126.
(44) Vasudevan, M.; Ajithkumar, P. S.; Singh, R. P.; Natarajan, N. Mass transfer kinetics using two-site interface model for removal of Cr(VI) from aqueous solution with cassava peel and rubber tree bark as adsorbents. *Environ. Eng. Res.* **2016**, *21*, 152−163.
(45) Jang, H. M.; Yoo, S.; Choi, Y.-K.; Park, S.; Kan, E. Adsorption isotherm, kinetic modeling and mechanism of tetracycline on Pinus taeda-derived activated biochar. *Bioresour. Technol.* **2018**, *259*, 24−31.
(46) Huang, Q.; Song, S.; Chen, Z.; Hu, B.; Chen, J.; Wang, X. Biochar-based materials and their applications in removal of organic contaminants from wastewater: state-of-the-art review. *Biochar* **2019**, *1*, 45−73.

https://dx.doi.org/10.1021/acsomega.9b03787
ACS Omega 2020, 5, 5748−5755